

DRAFT VERSION JUNE 11, 2019
Typeset using L^AT_EX **modern** style in AASTeX62

Understanding Heating in Active Region Cores through Machine Learning I. Numerical Modeling and Predicted Observables

W. T. BARNES,^{1,2,3} S. J. BRADSHAW,¹ AND N. M. VIAL⁴

¹*Department of Physics & Astronomy, Rice University, Houston, TX 77005-1827*

²*Lockheed Martin Solar & Astrophysics Laboratory, Palo Alto, CA 94304*

³*Bay Area Environmental Research Institute, Moffett Field, CA 94952*

⁴*NASA Goddard Space Flight Center, Greenbelt, MD 20771*

(Received 20 March 2019; Revised 29 May 2019; Accepted 7 June 2019)

Submitted to The Astrophysical Journal

ABSTRACT

To adequately constrain the frequency of energy deposition in active region cores in the solar corona, systematic comparisons between detailed models and observational data are needed. In this paper, we describe a pipeline for forward modeling active region emission using magnetic field extrapolations and field-aligned hydrodynamic models. We use this pipeline to predict time-dependent emission from active region NOAA 1158 as observed by SDO/AIA for low-, intermediate-, and high-frequency nanoflares. In each pixel of our predicted multi-wavelength, time-dependent images, we compute two commonly-used diagnostics: the emission measure slope and the time lag. We find that signatures of the heating frequency persist in both of these diagnostics. In particular, our results show that the distribution of emission measure slopes narrows and the mean decreases with decreasing heating frequency and that the range of emission measure slopes is consistent with past observational and modeling work. Furthermore, we find that the time lag becomes increasingly spatially coherent with decreasing heating frequency while the distribution of time lags across the whole active region becomes more broad with increasing heating frequency. In a follow up paper, we train a random forest classifier on these predicted diagnostics and use this model to classify real AIA observations of NOAA 1158 in terms of the underlying heating frequency.

Keywords: Sun:corona, Sun:UV radiation, methods:numerical, hydrodynamics

Corresponding author: W. T. Barnes
barnes@lmsal.com

1. INTRODUCTION

Nanoflares, energetic bursts of order 10^{24} erg resulting from small-scale reconnection (Parker 1988), have long been used to explain the observed million-degree temperatures in the non-flaring solar corona. Due to their faint, transient nature, direct observations of nanoflares are made difficult by several factors, including inadequate spectral coverage of instruments, the efficiency of thermal conduction, and non-equilibrium ionization (Cargill 1994; Winebarger et al. 2012; Barnes et al. 2016a). However, recent observations of “very hot” 8-10 MK plasma, the so-called “smoking gun” of nanoflares, have provided compelling evidence for their existence (e.g. Brosius et al. 2014; Caspi et al. 2015; Parenti et al. 2017; Ishikawa et al. 2017).

Critical to understanding the underlying heating mechanism is knowing whether the corona in non-flaring active regions is heated *steadily* or *impulsively*. However, because both waves and reconnection can lead to impulsive heating (Klimchuk 2015), it is better to ask at what frequency do nanoflares repeat on a given magnetic strand. In the case of low-frequency nanoflares, the time between consecutive events on a strand is long relative to its characteristic cooling time, giving the strand time to fully cool and drain before it is re-energized. In the high-frequency scenario, the time between events is short relative to the cooling time such that the strand is not allowed to fully cool before being heated again. Steady heating may be regarded as nanoflare heating in the very high-frequency limit.

Before proceeding, we note that a magnetic *strand*, the fundamental unit of the low- β corona, is a flux tube oriented parallel to the magnetic field that is isothermal in the direction perpendicular to magnetic field. We make the distinction that a *coronal loop* is an observationally-defined feature representing a field-aligned intensity enhancement relative to the surrounding diffuse emission, such that a single coronal loop may be composed of many thermally-isolated strands. Furthermore, we define the active region *core* as the area near the center of the active region whose X-ray and EUV emission is dominated by closed loops with both footpoints rooted in the photosphere within the active region.

In lieu of a direct observable signature of nanoflare heating, two parameters in particular have been used to diagnose the heating frequency in active region cores: the emission measure slope and the time lag. These diagnostics provide *indirect* signatures of the energy deposition via observations of the plasma cooling by thermal conduction, enthalpy, and radiation. We now discuss each of these observables in detail.

The emission measure distribution, $EM(T) = \int dh n_e^2$, where n_e is the electron density and the integration is taken along the line of sight, is a useful diagnostic for parameterizing the frequency of energy deposition. Many observational and theoretical studies have suggested that the “cool” portion of the $EM(T)$ (i.e. leftward of the peak, $10^{5.5} \lesssim T \lesssim 10^{6.5}$ K), can be described by $EM(T) \sim T^a$ (Jordan 1976; Cargill 1994; Cargill & Klimchuk 2004). The so-called *emission measure slope*, a ,

is an important diagnostic for assessing how often a single strand may be reheated and has been used by several researchers to interpret active region core observations in terms of both high- and low-frequency heating (see Table 3 of Bradshaw et al. 2012, and references therein). The “cool” emission measure slope typically falls in the range $2 < a < 5$, with shallower slopes indicative of low-frequency heating and steeper slopes associated with high-frequency heating. Many observational studies of active region cores have used the emission measure slope to make conclusions about the heating frequency (e.g. Tripathi et al. 2011; Warren et al. 2011; Winebarger et al. 2011; Schmelz & Pathak 2012; Warren et al. 2012; Del Zanna et al. 2015).

To better understand observable properties of nanoflare heating, several researchers have used hydrodynamic models of coronal loops to examine how the emission measure slope varies with heating frequency (e.g. Mulu-Moore et al. 2011; Bradshaw et al. 2012; Reep et al. 2013). Most recently, Cargill (2014) found that varying the time between consecutive heating events from 250 s (high-frequency heating) to 5000 s (low-frequency heating) could account for the wide observed distribution of emission measure slopes, with higher values of a corresponding to higher heating frequency due to the $EM(T)$ distribution becoming increasingly isothermal (see also Barnes et al. 2016b).

In addition to the emission measure slope, the time lag analysis of Viall & Klimchuk (2012) has also been used by several workers to understand the frequency of energy release in active region cores. The *time lag* is the temporal delay which maximizes the cross-correlation between two time series, and, qualitatively, can be thought of as the amount of time which one signal must be shifted relative to another in order to achieve the best “match” between the two signals. As the plasma cools through the six EUV channels of the Atmospheric Imaging Assembly instrument (AIA, Lemen et al. 2012) onboard the Solar Dynamics Observatory spacecraft (SDO, Pesnell et al. 2012), we expect to see the intensity peak in successively cooler passbands of AIA according to the sensitivity of each channel in temperature space (Viall & Klimchuk 2011). Computing the time lag between light curves in different channels provides a proxy for the cooling time between channels and insight into the thermal evolution of the plasma. Calculating the time lag in each pixel of an AIA image can reveal large scale cooling patterns in coronal loops as well as the diffuse emission between loops across an entire active region.

Viall & Klimchuk (2012) computed time lags for all possible AIA EUV channel pairs in every pixel of active region NOAA 11082 and found positive time lags across the entire active region core, indicative of cooling plasma. They interpreted these observations as being inconsistent with a steady heating model. Viall & Klimchuk (2017) extended this analysis to the 15 active regions catalogued by Warren et al. (2012) and found overwhelmingly positive time lags, or cooling plasma, in all cases, with only a few isolated instances of negative time lags, or heating plasma. These observations are consistent with an impulsive heating scenario in which little emission

is produced during the heating phase because of the time needed to fill the corona by chromospheric evaporation and the efficiency of thermal conduction. [Bradshaw & Viall \(2016\)](#) predicted AIA intensities for a range of nanoflare heating frequencies in a model active region and applied the time lag analysis to their simulated images. They found that aspects of both high- and intermediate-frequency nanoflares reproduced the observed time lag patterns, but neither model could fully account for the observational constraints, suggestive of a range of heating frequencies across the active region. Additionally, [Lionello et al. \(2016\)](#) used a field-aligned hydrodynamic model to compute time lags for several loops in NOAA 11082 and concluded that an impulsive heating model could not account for the long (> 5000 s) time lags calculated from observations by [Viall & Klimchuk \(2012\)](#).

Any successful heating model must be able to reproduce the observed distribution of emission measure slopes and time lags. In order to carry out such a test, both advanced forward modeling and sophisticated comparisons to data are required. In this paper, we carry out a series of nanoflare heating simulations in order to better understand how the frequency of impulsive heating events on a given strand is related to observable properties of the plasma, notably the emission measure slope and the time lag as derived from AIA observations. To do this, we use a combination of magnetic field extrapolations, hydrodynamic models, and atomic data to produce simulated AIA emission which can be treated in the same manner as real observations. We then apply the emission measure and time lag analyses to this simulated data. [Section 2](#) provides a detailed description of both our forward modeling pipeline and the nanoflare heating model. In [Section 3](#), we show the predicted intensities for each heating model and AIA channel ([Section 3.1](#)), the resulting emission measure slopes ([Section 3.2.1](#)) and the time lags ([Section 3.3](#)). [Section 4](#) provides some discussion of our results and [Section 5](#) includes a summary and concluding remarks.

This paper is the first in a series concerned with constraining nanoflare heating properties through forward modeled observables and serves to describe our forward modeling pipeline and lay out the results of our nanoflare simulations. In [Barnes et al. \(2019, Paper II hereafter\)](#), we use machine learning to make detailed comparisons to AIA observations of active region NOAA 1158. We train a random forest classifier using the predicted emission measure slopes and time lags presented here over the entire heating frequency parameter space in order to classify the heating frequency in each pixel of the observed active region. In contrast to past studies which have relied on a single diagnostic, this approach allows us to simultaneously account for an arbitrarily large number of observables in deciding which model fits the data “best.” The ability to quantitatively compare models with large quantities of data is crucial for progress in the current era where the amount of solar coronal data is orders of magnitude larger than in the past. Combined, these two papers demonstrate a novel method for using real and simulated observations to systematically predict heating properties in active region cores.

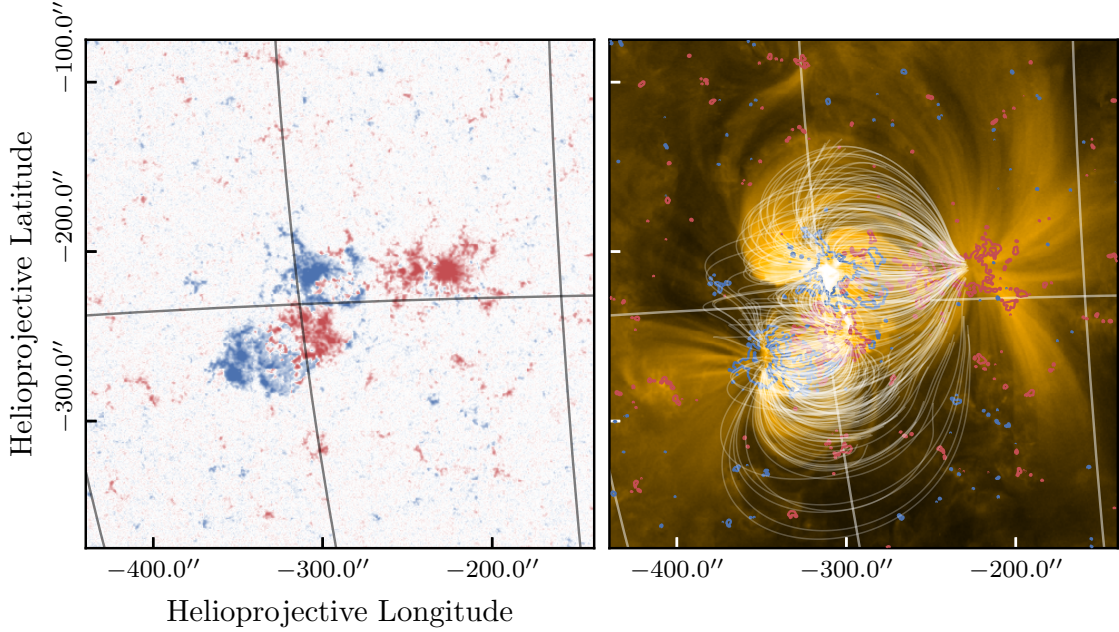


Figure 1. Active region NOAA 1158 on 12 February 2011 15:32:42 UTC as observed by HMI (left) and the 171 Å channel of AIA (right). The gridlines show the heliographic longitude and latitude. The left panel shows the LOS magnetogram and the colorbar range is ± 750 G on a symmetrical log scale. In the right panel, 500 out of the total 5000 field lines are overlaid in white and the red and blue contours show the HMI LOS magnetogram at the +5% (red) and -5% (blue) levels.

2. MODELING

In order to understand how signatures of the heating frequency are manifested in the emission measure slope and time lag, we predict the emission over the entire active region as observed by SDO/AIA for a range of nanoflare heating frequencies. To do this, we have constructed an advanced forward modeling pipeline through a combination of magnetic field extrapolations, field-aligned hydrodynamic simulations, and atomic data¹. In the following section, we discuss each step of our pipeline in detail.

2.1. Magnetic Field Extrapolation

We choose active region NOAA 1158, as observed by the Helioseismic Magnetic Imager (HMI, Scherrer et al. 2012) on 12 February 2011 15:32:42 UTC, from the list of active regions studied by Warren et al. (2012). The line-of-sight (LOS) magnetogram is shown in the left panel of Figure 1. We model the geometry of active region NOAA 1158 by computing the three-dimensional magnetic field using the oblique potential field extrapolation method of Schmidt (1964) as outlined in Sakurai (1982, Section 3). The extrapolation technique of Schmidt is well-suited for our purposes due to

¹ Our forward modeling pipeline, called synthesizAR, is modular and flexible and written entirely in Python. The complete source code, along with installation instructions and documentation, are available here: github.com/wtbarnes/synthesizAR

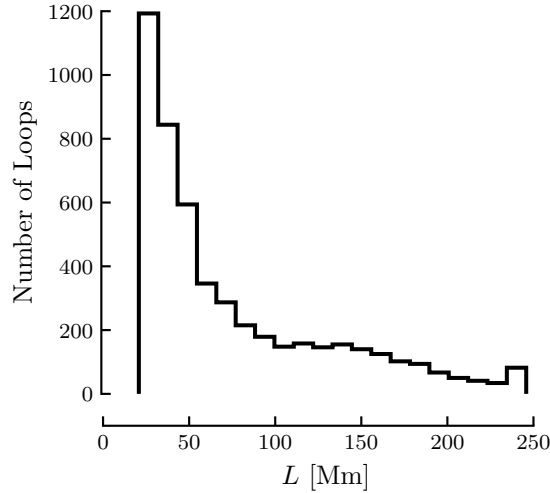


Figure 2. Distribution of footpoint-to-footpoint lengths (in Mm) of the 5000 field lines traced from the field extrapolation computed from the magnetogram of NOAA 1158.

its simplicity and efficiency though we note it is only applicable on the scale of an active region. We include the oblique correction to account for the fact that the active region is off of disk-center.

The HMI LOS magnetogram provides the lower boundary condition of the vector magnetic field (i.e. $B_z(x, y, z = 0)$) for our field extrapolation. We crop the magnetogram to an area of $300''$ -by- $300''$ centered on $(-288.26'', -223.21'')$ and resample the image to 100-by-100 pixels to reduce the computational cost of the field extrapolation. Additionally, we define our extrapolated field to have a dimension of 100 pixels and spatial extent of $0.3R_\odot$ in the z -direction such that each component of our extrapolated vector magnetic field \vec{B} has dimensions (100, 100, 100).

After computing the three-dimensional vector field from the observed magnetogram, we trace 5×10^3 field lines through the extrapolated volume using the streamline tracing functionality in the yt software package (Turk et al. 2011). We choose 5×10^3 lines in order to balance computational cost with the need to make the resulting emission approximately volume filling. We place the seed points for the field line tracing at the lower boundary ($z = 0$) of the extrapolated vector field in areas of strong, positive polarity in B_z . Furthermore, we keep only closed field lines in the range $20 < L < 300$ Mm, where L is the full length of the field line. The right panel of Figure 1 shows a subset of the traced field lines overlaid on the observed AIA 171 Å image of NOAA 1158. Contours from the observed HMI LOS magnetogram are shown in red (positive polarity) and blue (negative polarity). A qualitative comparison between the extrapolated field lines and the loops visible in the AIA 171 Å image reveals that the field extrapolation and line tracing adequately capture the three-dimensional geometry of the active region. Figure 2 shows the distribution of footpoint-to-footpoint lengths for all of the traced field lines.

2.2. Hydrodynamic Modeling

Due to the low- β nature of the corona, we can treat each field line traced from the field extrapolation as a thermally-isolated strand. We use the Enthalpy-based Thermal Evolution of Loops model (EBTEL, Klimchuk et al. 2008; Cargill et al. 2012a,b), specifically the two-fluid version of EBTEL (Barnes et al. 2016a), to model the thermodynamic response of each strand. The two-fluid EBTEL code solves the time-dependent, two-fluid hydrodynamic equations spatially-integrated over the corona for the electron pressure and temperature, ion pressure and temperature, and density. The two-fluid EBTEL model accounts for radiative losses in both the transition region and corona, thermal conduction (including flux limiting), and binary Coulomb collisions between electrons and ions. The time-dependent heating input is configurable and can be deposited in the electrons and/or ions. A detailed description of the model and a complete derivation of the two-fluid EBTEL equations can be found in Appendix B of Barnes et al. (2016a).

For each of the 5×10^3 strands, we run a separate instance of the two-fluid EBTEL code for 3×10^4 s of simulation time to model the time-dependent, spatially-averaged coronal temperature and density. For each simulation, the loop length is determined from the field extrapolation. We include flux limiting in the heat flux calculation and use a flux limiter constant of 1 (see Equations 21 and 22 of Klimchuk et al. 2008). Additionally, we choose to deposit all of the energy into the electrons though we note that preferentially energizing one species over another will not significantly impact the cooling behavior of the loop as the two species will have had sufficient time to equilibrate (Barnes et al. 2016a,b). To map the results back to the extrapolated field lines, we assign a single temperature and density to every point along the strand at each time step. Though EBTEL only computes spatially-averaged quantities in the corona, its efficiency allows us to calculate time-dependent solutions for many thousands of strands in a few minutes.

2.3. Heating Model

We parameterize the heating input in terms of discrete heating pulses on a single strand with triangular profiles of duration $\tau_{\text{event}} = 200$ s. For each event i , there are two parameters: the peak heating rate q_i and the waiting time prior to the event $t_{\text{wait},i}$. We define the waiting time such that $t_{\text{wait},i}$ is the amount of time between when event $i - 1$ ends and event i begins. Following the approach of Cargill (2014), we relate the waiting time and the event energy such that $t_{\text{wait},i} \propto q_i$. The physical motivation for this scaling is as follows. In the nanoflare model of Parker (1988), random convective motions continually stress the magnetic field rooted in the photosphere, leading to the buildup and eventual release of energy. If the field is stressed for a long amount of time without relaxation, large discontinuities will have time to develop in the field, leading to a dramatic release of energy. Conversely, if the field relaxes quickly, there is

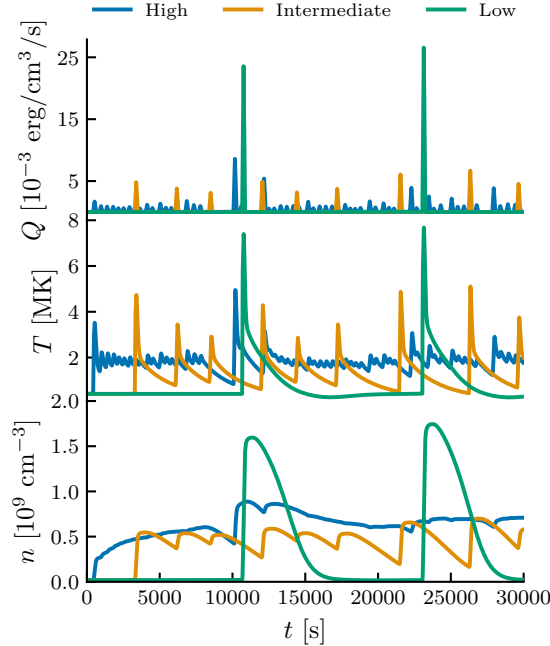


Figure 3. Heating rate (top), electron temperature (middle), and density (bottom) as a function of time for the three heating scenarios for a single strand. The colors denote the heating frequency as defined in the legend. The strand has a half length of $L/2 \approx 40$ Mm and a mean field strength of $\bar{B} \approx 30$ G.

not enough time for the field to become sufficiently stressed and the resulting energy release will be relatively small.

In this work we explore three different heating scenarios: low-, intermediate-, and high-frequency nanoflares. We define the heating frequency in terms of the ratio between the fundamental cooling timescale due to thermal conduction and radiation, τ_{cool} , and the average waiting time of all events on a given strand, $\langle t_{\text{wait}} \rangle$,

$$\varepsilon = \frac{\langle t_{\text{wait}} \rangle}{\tau_{\text{cool}}} \begin{cases} < 1, & \text{high frequency,} \\ \sim 1, & \text{intermediate frequency,} \\ > 1, & \text{low frequency.} \end{cases} \quad (1)$$

We choose to parameterize the heating in terms of the cooling time rather than an absolute waiting time as $\tau_{\text{cool}} \sim L$ (see appendix of [Cargill 2014](#)). While a waiting time of 2000 s might correspond to low-frequency heating for a 20 Mm strand, it would correspond to high-frequency heating in the case of a 150 Mm strand. By parameterizing the heating in this way, we ensure that all strands in the active region are heated at the same frequency relative to their cooling time. [Figure 3](#) shows the heating rate, electron temperature, and density as a function of time, for a single strand, for the three heating scenarios listed above.

For a single impulsive event i with a triangular temporal profile of duration τ_{event} , the energy density is $E_i = \tau_{\text{event}} q_i / 2$. Summing over all events on all strands that

Table 1. All three heating models plus the two single-event control models. In the single-event models, the energy flux is not constrained by Equation 3.

Name	ε (see Eq.1)	Energy Constrained?
high	0.1	yes
intermediate	1	yes
low	5	yes
cooling	1 event per strand	no
random	1 event per strand	no

comprise the active region gives the total energy flux injected into the active region,

$$F_{AR} = \frac{\tau_{\text{event}}}{2} \frac{\sum_l^{N_{\text{strands}}} \sum_i^{N_l} q_i L_l}{t_{\text{total}}} \quad (2)$$

where t_{total} is the total simulation time, N_{strands} is the total number of strands comprising the active region, and $N_l = (t_{\text{total}} + \langle t_{\text{wait}} \rangle) / (\tau + \langle t_{\text{wait}} \rangle)$ is the total number of events occurring on each strand over the whole simulation. Note that the number of events per strand is a function of both ε and τ_{cool} .

For each heating frequency, we constrain the total flux into the active region to be $F_* = 10^7 \text{ erg cm}^{-2} \text{ s}^{-1}$ (Withbroe & Noyes 1977) such that F_{AR} must satisfy the condition,

$$\frac{|F_{AR}/N_{\text{strands}} - F_*|}{F_*} < \delta, \quad (3)$$

where $\delta \ll 1$. For each strand, we choose N_l events each with energy E_i from a power-law distribution with slope -2.5 and fix the upper bound of the distribution to be $\bar{B}_l^2/8\pi$, where \bar{B}_l is the spatially-averaged field strength along the strand l as derived from the field extrapolation. This is the maximum amount of energy made available by the field to heat the strand. We then iteratively adjust the lower bound on the power-law distribution for E_i until we have satisfied Equation 3 within some numerical tolerance. We note that the set of E_i we choose for each strand may not uniquely satisfy Equation 3.

We use the field strength derived from the potential field extrapolation to constrain the energy input to our hydrodynamic model for each strand. While the derived potential field is already in its lowest energy state and thus has no energy to give up, our goal here is only to understand how the distribution of field strength may be related to the properties of the heating. In this way, we use the potential field as a proxy for the non-potential component of the coronal field, with the understanding that we cannot make any quantitative conclusions regarding the amount of available energy or the stability of the field itself.

In addition to these three multi-event heating models, we also run two single-event control models. In both control models every strand in the active region is heated

exactly once by an event with energy $\bar{B}_l^2/8\pi$. In our first control model, the start time of every event is $t = 0$ s such that all strands are allowed to cool uninterrupted for $t_{\text{total}} = 10^4$ s. In the second control model, the start time of the event on each strand is chosen from a uniform distribution over the interval $[0, 3 \times 10^4]$ s, such that the heating is likely to be out of phase across all strands. In these two models, the energy has not been constrained according to Equation 3 and the total flux into the active region is $(\sum_l \bar{B}_l^2 L_l)/8\pi t_{\text{total}}$. From here on, we will refer to these two models as the “cooling” and “random” models, respectively. All five heating scenarios are summarized in Table 1.

2.4. Forward Modeling

2.4.1. Atomic Physics

For an optically-thin, high-temperature, low-density plasma, the radiated power per unit volume, or *emissivity*, of a transition λ_{ij} of an electron in ion k of element X is given by,

$$P(\lambda_{ij}) = \frac{n_H}{n_e} \text{Ab}(X) N_j(X, k) f_{X,k} A_{ji} \Delta E_{ji} n_e, \quad (4)$$

where N_j is the fractional energy level population of excited state j , $f_{X,k}$ is the fractional population of ion k , $\text{Ab}(X)$ is the abundance of element X relative to hydrogen, $n_H/n_e \approx 0.83$ is the ratio of hydrogen and electron number densities, A_{ji} is the Einstein coefficient, and $\Delta E_{ji} = hc/\lambda_{ij}$ is the energy of the emitted photon (see Mason & Fossi 1994; Del Zanna & Mason 2018). To compute Equation 4, we use version 8.0.6 of the CHIANTI atomic database (Dere et al. 1997; Young et al. 2016). We use the abundances of Feldman et al. (1992) as provided by CHIANTI. For each atomic transition, A_{ji} and λ_{ji} can be looked up in the database. To find N_j , we solve the level-balance equations for ion k , including the relevant excitation and de-excitation processes as provided by CHIANTI (see Section 3.3 of Del Zanna & Mason 2018).

The ion population fractions, $f_{X,k}$, provided by CHIANTI assume ionization equilibrium (i.e. the ionization and recombination rates are always in balance). However, in the rarefied solar corona, where the plasma is likely heated impulsively, it is not guaranteed that the ionization timescale is less than the heating timescale such that the ionization state may not be representative of the electron temperature (Bradshaw & Cargill 2006; Reale & Orlando 2008; Bradshaw 2009). To properly account for this effect, we compute $f_{X,k}$ by solving the time-dependent ion population equations for each element using the ionization and recombination rates provided by CHIANTI. The details of this calculation are provided in Appendix A.

2.4.2. Instrument Effects

We combine Equation 4 with the wavelength response function of the instrument to model the intensity as it would be observed by AIA,

$$I_c = \frac{1}{4\pi} \sum_{\{ij\}} \int_{\text{LOS}} dh P(\lambda_{ij}) R_c(\lambda_{ij}) \quad (5)$$

Table 2. Elements included in the calculation of Equation 5. For each element, we include all ions for which CHIANTI provides sufficient data for computing the emissivity.

Element	Number of Ions	Number of Transitions
O	8	11892
Mg	11	31965
Si	13	30047
S	16	33091
Ca	17	42823
Fe	25	553541
Ni	19	83517

where I_c is the intensity for a given pixel in channel c , $P(\lambda_{ij})$ is the emissivity as given by Equation 4, R_c is the wavelength response function of the instrument for channel c (see Boerner et al. 2012), $\{ij\}$ is the set of all atomic transitions listed in Table 2, and the integration is along the LOS. Note that when computing the intensity in each channel of AIA, we do not rely on the temperature response functions computed by SolarSoft (SSW, Freeland & Handy 1998) and instead use the wavelength response functions directly. This is because the response functions returned by `aia_get_response.pro` assume both ionization equilibrium and constant pressure. Appendix B provides further details on our motivation for recomputing the temperature response functions.

We compute the emissivity according to Equation 4 for all of the transitions in Table 2 using the temperatures and densities from our hydrodynamic models for all 5×10^3 strands. We then compute the LOS integral in Equation 5 by first converting the coordinates of each strand to a helioprojective (HPC) coordinate frame (see Thompson 2006) using the coordinate transformation functionality in Astropy (The Astropy Collaboration et al. 2018) combined with the solar coordinate frames provided by SunPy (SunPy Community et al. 2015). This enables us to easily project our simulated active region along any arbitrary LOS simply by changing the location of the observer that defines the HPC frame. Here, our HPC frame is defined by an observer at the position of the SDO spacecraft on 12 February 2011 15:32:42 UTC (i.e. the time of the HMI observation of NOAA 1158 shown in Figure 1).

Next, we use these transformed coordinates to compute a weighted two-dimensional histogram, using the integrand of Equation 5 at each coordinate as the weights. We construct the histogram such that the bin widths are consistent with the spatial resolution of the instrument. For AIA, a single bin, representing a single pixel, has a width of $0.6''$ -per-pixel. Finally, we apply a gaussian filter to the resulting histogram to emulate the point spread function of the instrument. We do this for each time

step, using a cadence of 10 s, and for each channel. For every heating scenario, this produces approximately $6(3 \times 10^4)/10 \approx 2 \times 10^4$ separate images.

3. RESULTS

We forward model time-dependent AIA intensities using the method outlined in [Section 2.4](#) for the heating scenarios discussed in [Section 2.3](#). We discuss the predicted intensities in [Section 3.1](#) for all six EUV channels of AIA and all five heating models. In [Section 3.2](#) and [Section 3.3](#), we show the results of the emission measure and time lag analyses, respectively, as applied to our simulated data. In [Paper II](#), we use these simulated observables to train a machine learning classification model to understand with which heating scenario the real data are most consistent.

3.1. Intensities

We compute the intensities for the 94, 131, 171, 193, 211, and 335 Å channels of SDO/AIA using the procedure described in [Section 2.4](#). We compute the intensity in each pixel of the model active region over a total simulation period of 3×10^4 s ≈ 8.3 hours with the exception of the cooling case which is only run for 10^4 s. For the high-, intermediate-, low-frequency and “random” models, we discard the first and last 5×10^3 s of evolution to avoid any transient effects in the strand evolution associated with the initial conditions and the constraints placed on the energy, respectively. We complete this procedure for each of the five heating scenarios in [Table 1](#).

[Figure 4](#) shows a snapshot of the intensity map at $t = 15 \times 10^3$ s for each channel and for the high-, intermediate-, and low-frequency nanoflare heating cases. The rows correspond to the different heating scenarios while the columns show the six AIA EUV channels. In each column, the intensities are normalized to the maximum intensity in the low-frequency case and are on a square-root scale. In general, we find that in the high-frequency intensity maps, individual loops are difficult to distinguish while in the low-frequency case individual loops appear bright relative to the surrounding emission. This distinguishability or “fuzziness” can be measured quantitatively as σ_I/\bar{I} , where σ_I is the standard deviation taken over all pixels and \bar{I} is the mean intensity ([Guarrasi et al. 2010](#), Equation 11). A larger value of σ_I/\bar{I} indicates a greater degree of contrast and vice versa. σ_I/\bar{I} for each channel and heating frequency is shown in [Table 3](#). With the exception of 131 Å, for every channel, the high-frequency case is the most “fuzzy”. The low-frequency case shows the most contrast in each channel except 94 Å though the margin between the low and intermediate cases is quite small in some cases.

Looking at the first two columns of [Figure 4](#), we see that the intensity in the 94 and 131 Å channels increases as the heating frequency decreases. Both channels are double peaked and have “hot” (≈ 7 MK for 94 Å, ≈ 12 MK for 131 Å) and “warm” (≈ 1 MK for 94 Å, ≈ 0.5 MK for 131 Å) components. In the case of high-frequency heating, less energy is available per event such that few strands are heated to > 4 MK. There is little emission in the 131 Å channel as strands are not often permitted to cool

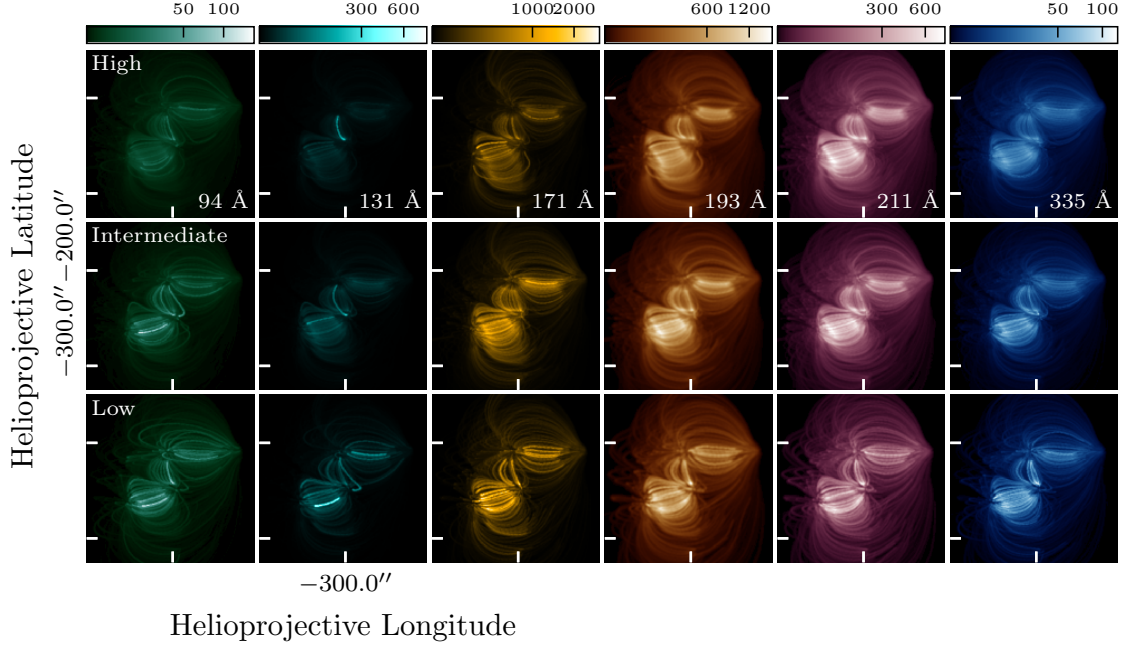


Figure 4. Snapshots of intensity, in $\text{DN pixel}^{-1} \text{s}^{-1}$, across the whole active region at $t = 15 \times 10^3 \text{ s}$. The rows correspond to the three different heating frequencies and the columns are the six EUV channels of AIA. In each column, the colorbar is on a square-root scale and is normalized between zero and the maximum intensity in the low-frequency case. The color tables are the standard AIA color tables as implemented in SunPy ([SunPy Community et al. 2015](#)).

Table 3. σ_I/\bar{I} as defined by Equation 11 of [Guarrasi et al. \(2010\)](#) computed on a single image at $t = 15 \times 10^3 \text{ s}$ for each channel and heating frequency. A larger value denotes a greater degree of contrast.

Channel [\AA]	High	Intermediate	Low
94	3.06	4.63	4.19
131	5.56	3.61	6.13
171	2.79	2.81	3.25
193	2.69	2.80	2.79
211	2.73	2.83	2.84
335	2.63	3.08	3.21

to $\leq 0.5 \text{ MK}$ either. However, in the low- and intermediate-frequency cases, we see several individual bright loops in both the 94 and 131 \AA channels as the heating rate is sufficient to produce “hot” (i.e. 8-10 MK) loops. We see only a few of these loops as the lifetime of this hot plasma is short due to the efficiency of thermal conduction.

In contrast, the faint, diffuse component of the 94 Å emission that is present in all three cases is due to the contribution of the “warm” component.

Additionally, we find that the 171 Å channel is dimmer for high-frequency heating as the peak sensitivity of this channel is < 1 MK and in the case of high-frequency heating, strands are rarely allowed to cool below 1 MK. In contrast, we note that the overall intensity in the 193, 211, and 335 Å channels is relatively constant over heating frequency as compared to the three previous channels though individual loops do become more visible with decreasing heating frequency. This relative insensitivity is because the temperature response functions of these three channels all peak in between 1.5 MK and 2.5 MK. In the case of high-frequency heating, strands are being sustained near these temperatures while in the low-frequency case, strands are cooling through this temperature range. This is illustrated for a single strand in [Figure 3](#).

While there are clear differences in the AIA intensities between all three heating frequencies, quantifying these differences is difficult due in part to the multidimensional nature of the intensity data. To better understand how observational signatures differ as a function of heating frequency, we need to find a reduced representation of our data set that retains signatures of the underlying energy deposition. To this end, we compute two common observables: the emission measure slope ([Section 3.2](#)) and the time lag ([Section 3.3](#)).

3.2. Emission Measure Distributions

As discussed in [Section 1](#), the emission measure slope is a useful quantity for understanding how frequently strands are re-energized. We compute emission measure distributions from our forward-modeled intensities using the regularized inversion method of [Hannah & Kontar \(2012\)](#). This method was designed to work with the narrowband coverage provided by AIA and so is well-suited to our needs. We choose our temperature bins such that the leftmost edge is at $10^{5.5}$ K and the rightmost edge at $10^{7.2}$ K with bin widths of $\Delta \log T = 0.1$. Rather than computing $\text{EM}(T)$ at each time step, we compute the time-averaged intensity in each pixel of each channel and compute $\text{EM}(T)$ only once. We compute the uncertainties on the intensities in each channel using the `aia_bp_estimate_error.pro` procedure in SSW which incorporates uncertainties due to shot noise, read noise, dark subtraction, quantization, photometric calibration, and onboard compression.

[Figure 5](#) shows the emission measure distribution, $\text{EM}(T)$, for the case of high-, intermediate-, and low-frequency nanoflares. The three panels correspond to the three locations marked in [Figure 6](#). The dashed lines in each panel denote the location of T_{peak} , where $T_{\text{peak}} = \text{argmax}_T \text{EM}(T)$ is the temperature at which the emission measure distribution is maximum. At each sample location, the $\text{EM}(T)$ becomes increasingly narrow with increasing heating frequency. We find that T_{peak} is between ≈ 2 MK and 4 MK in all cases and is lowest at point C near the periphery of the

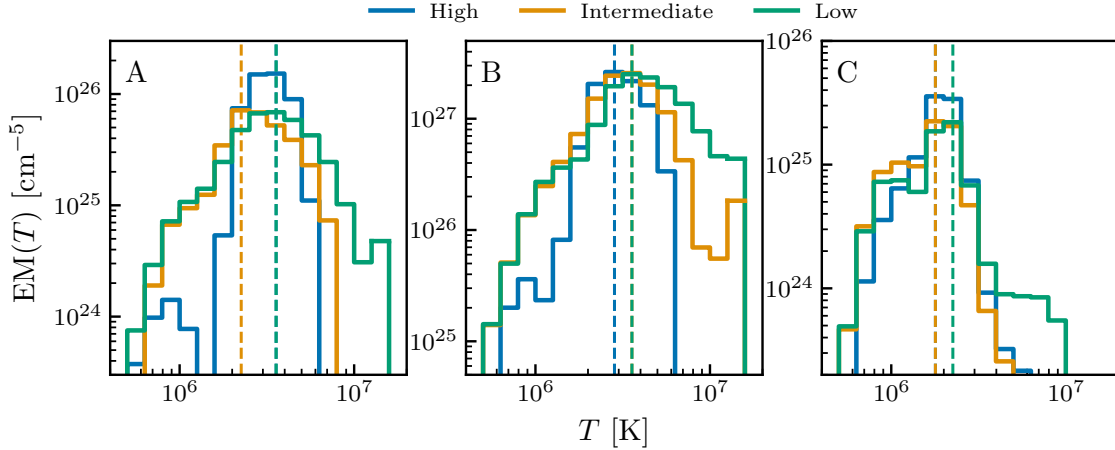


Figure 5. $EM(T)$ at three different locations in the active region for all three heating frequencies. The dashed vertical lines denote the value of T_{peak} . Each panel corresponds to a different pixel in the active region as denoted by the label in the top left corner. The locations of these three pixels are marked with their corresponding labels in Figure 6.

active region where the loops are the longest. We note that in all cases, T_{peak} is significantly below 4 MK, the value measured by Warren et al. (2012) from spectroscopic observations of this same active region. However, we note that at point B, the location closest to that at which Warren et al. computed their $EM(T)$ distributions, we find the highest T_{peak} , between ≈ 3 MK and 4 MK.

3.2.1. Emission Measure Slopes

After computing $EM(T)$ in each pixel using the regularized inversion procedure, we fit a first-order polynomial to the log-transformed emission measure and temperature bin centers, $\log_{10} EM \sim a \log_{10} T$, to calculate the emission measure slope, a . In Paper II, we compare our modeled emission measure slopes to those derived from real AIA observations of NOAA 1158 using this same method.

Figure 6 shows the resulting emission measure slope, a , in each pixel of our forward-modeled active region for the high-, intermediate-, and low-frequency cases. We fit $EM(T)$ over bins in the temperature range $8 \times 10^5 \text{ K} \leq T < T_{\text{peak}}$. To assess the “goodness-of-fit” we use r^2 , the correlation coefficient for the first-order polynomial fit, and mask pixels with $r^2 < 0.75$. Looking at the three panels in Figure 6, we find that overall, a tends to decrease with decreasing frequency, consistent with previous modeling work (see Section 1). The low-frequency map (right panel) shows many values close to 2.

As the heating frequency increases, the slopes become larger, indicating an increasingly isothermal emission measure distribution. The intermediate-frequency map (center panel) shows predominantly higher slopes, with most pixels in the range $2 \lesssim a \lesssim 3.5$ while the high-frequency map (left panel) shows much steeper slopes, with many $a \geq 3.5$, and a much broader range of slopes, $3 \lesssim a \lesssim 8$. Note that in the high-frequency case, the slope varies considerably across the active region while

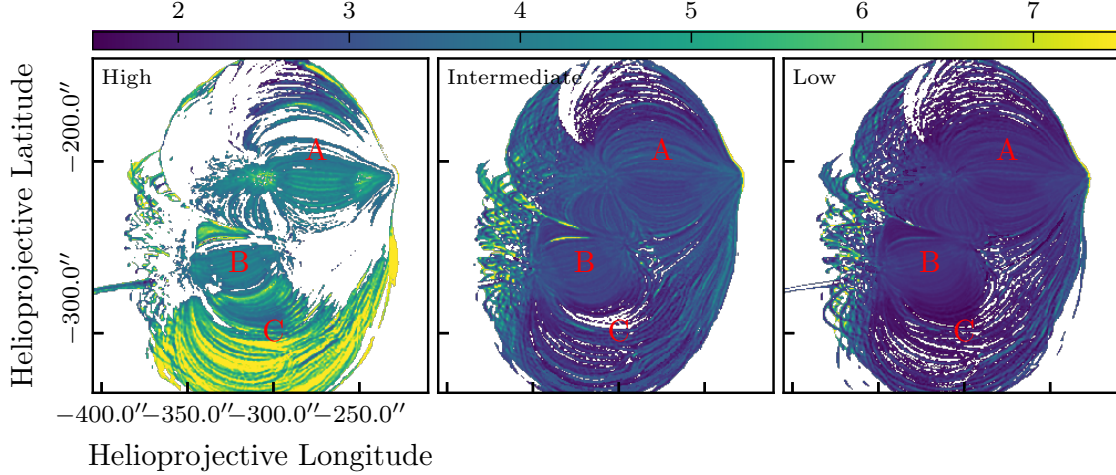


Figure 6. Maps of the emission measure slope, a , in each pixel of the active region for the high- (left), intermediate- (center), and low-frequency (right) cases. The $EM(T)$ is computed using time-averaged intensities from the six AIA EUV channels using the method of [Hannah & Kontar \(2012\)](#). The $EM(T)$ in each pixel is then fit to T^a over the temperature range $8 \times 10^5 \text{ K} \leq T < T_{\text{peak}}$. Any pixels with $r^2 < 0.75$ are masked and colored white. The red labels in each panel denote the three locations at which the $EM(T)$ distributions in [Figure 5](#) were calculated.

the distribution of a appears more spatially uniform in the intermediate- and low-frequency cases.

Below T_{peak} , [Cargill \(1994\)](#) noted that the $EM(T)$ could be described by $EM(T) \sim n^2 \tau_{\text{rad}}$, where $\tau_{\text{rad}} \sim T^{1-\alpha} n^{-1}$ is the radiative cooling time and α determines the temperature dependence of the radiative loss function. Assuming $T \propto n^2$ ([Serio et al. 1991](#); [Jakimiec et al. 1992](#)) and approximating the temperature dependence of the radiative losses as $\alpha = -1/2$ ([Cargill 1994](#); [Cargill et al. 1995](#)) gives $a \approx 2$. We find that emission measure slopes produced by low-frequency nanoflares as shown in the right panel of [Figure 6](#) are approximately consistent with analytical results for single nanoflares though many of the low-frequency slopes are > 2 . This is likely due to the omission of enthalpy-driven cooling in the above scaling relation. [Bradshaw & Cargill \(2010\)](#) found $T \sim n^\ell$, with $\ell \approx 1$ for long loops, where enthalpy-driven cooling is likely to dominate over radiative losses, and $\ell \approx 2$ for shorter loops, where radiation remains the dominant cooling mechanism. Thus, the distribution of a will depend on the distribution of loop lengths and smaller values of ℓ will lead to larger emission measure slopes (e.g. $a = 2.5$ for $\ell = 1$).

3.2.2. Histograms

[Figure 7](#) shows histograms of the emission measure slopes for the high-, intermediate-, and low-frequency cases. We find that the low-frequency distribution peaks at $a \approx 2.3$, inside the range expected from analytical results as noted above. The intermediate- and high-frequency distributions peak at successively higher values, ≈ 2.8 and ≈ 4.0 , respectively. While the low- and intermediate-frequency distribu-

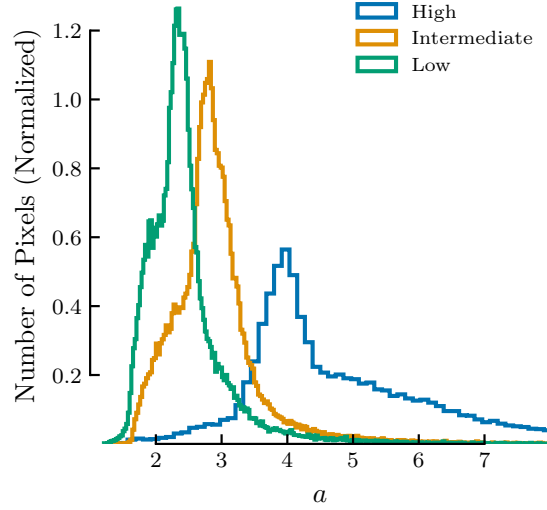


Figure 7. Distribution of emission measure slopes, a , for every pixel in the simulated active region for the high-, intermediate-, and low-frequency heating scenarios as shown in Figure 6. The histogram bins are determined using the Freedman Diaconis estimator (Freedman & Diaconis 1981) as implemented in the Numpy package for array computation in Python (Oliphant 2006) and each histogram is normalized such that the area under the histogram is equal to 1.

tions are more narrowly distributed around their peak values, the distribution of slopes in the high-frequency case is relatively broad and has a positive skew towards steeper slopes.

Looking at the distribution of slopes across the entire active region in Figure 7, we find that when the strands are heated infrequently such that each strand is allowed to cool fully prior to the next event, the distribution of slopes “saturates” in the range expected for single nanoflares. However, as the heating frequency increases and the strands are reheated more often, the value of the slope becomes unsaturated and is subject to a wide range of cooling times due to the dependence of each waiting time on the power-law heating rate (see Section 2.3). These results are consistent with Cargill (2014) who computed $EM(T) = n^2 L$ for a single strand for a range of heating frequencies and found a converged to ≈ 2 for low frequency nanoflares and increased slowly with increasing heating frequency.

Our modeled emission measure slopes show that, even when accounting for the LOS integration, atomic physics, and information lost in the $EM(T)$ inversion, signatures of the heating frequency still persist in the emission measure slope. However, while this quantity retains information about the frequency of energy deposition, drawing conclusions about the heating based solely on the observed emission measure slope, particularly for a small number of pixels may be misleading. As shown here and in Del Zanna et al. (2015), the slope may vary significantly across a given active region. Additionally, calculating $EM(T)$ from observations is non-trivial due to several factors, including the mathematical difficulties of the ill-posed inversion (Craig &

Brown 1976; Judge et al. 1995, 1997), uncertainties in the atomic data (Guennou et al. 2013), and insufficient constraints from spectroscopic observations (e.g. Landi & Klimchuk 2010; Winebarger et al. 2012), among others.

3.3. Time Lags

Next, we apply the time lag method of Viall & Klimchuk (2012) to our synthetic intensities for all of the heating scenarios discussed in Section 2.3. For each pixel in the active region, we compute the cross-correlation (Equation C6) for all pairs of the EUV channels of AIA (15 in total) and find the temporal offset which maximizes the cross-correlation according to Equation C7. The details of the cross-correlation and time lag calculation are given in Appendix C. Using the convention of Viall & Klimchuk (2012), we order the channel pairs such that the “hot” channel is listed first, meaning that a positive time lag corresponds to variability in the hotter channel followed by variability in the cooler channel. In other words, *a positive time lag indicates cooling plasma*. For the 94 Å and 131 Å channels, both of which have a bimodal temperature response function (see Figure 11), the order is determined by the component which is most dominant such that 94 Å is ordered first while 131 Å is ordered second. Thus, it is possible for cooling plasma to produce negative time lags in these channel pairs and the ambiguity can be resolved in the context of the time lags in other channel pairs.

3.3.1. Time Lag Maps

Figure 8 shows τ_{AB} (Equation C7) in each pixel of our simulated active region for all heating scenarios listed in Table 1 and three selected channel pairs: 94-335 Å, 211-131 Å, and 193-171 Å. Blacks, blues, and greens correspond to negative time lags; reds, oranges, and yellows correspond to positive time lags; and olive green indicates zero time lag. The range of the colorbar is ± 6000 s. Note that the heating frequency decreases from left to right across each row. If the correlation in a given pixel is too low ($\max \mathcal{C}_{AB} < 0.1$), the pixel is masked and colored white.

Looking at the first two rows of Figure 8, we find that the positive time lags in the 211-131 Å channel pair are significantly longer than those in the 94-335 Å pair. In the temperature range $2.5 < T < 7.3$ MK (94-335 Å), the dominant cooling mechanism is field-aligned thermal conduction while radiative cooling dominates in the range $0.6 < T < 2.5$ MK (211-131 Å). Because thermal conduction is far more efficient at high temperatures, the plasma spends less time in the $[T_{335}, T_{94}]$ temperature range than in $[T_{131}, T_{211}]$. The 193-171 Å time lags for the cooling case fall in the middle as radiative cooling also tends to dominate in this temperature interval ($0.9 < T < 1.5$ MK), but the separation in temperature space is smaller than the 211-131 Å pair. In all cases, these differences in the magnitude of the positive time lags become more apparent at lower heating frequencies.

In the 94-335 Å pair, we find negative time lags in the longest loops near the edge of the active region, inconsistent with our previous assertion that longer loops lead

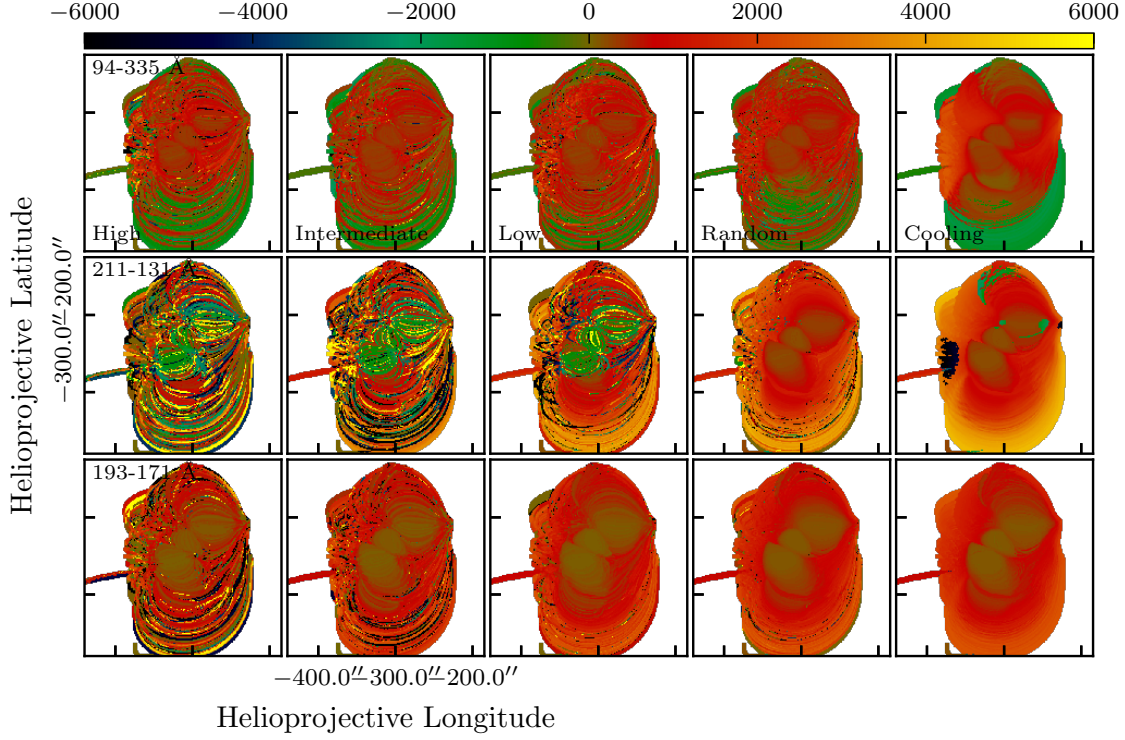


Figure 8. Time lag maps for three different channel pairs for all five of the heating scenarios described in Table 1. The value of each pixel indicates the temporal offset, in seconds, which maximizes the cross-correlation (Equation C7). The rows indicate the different channel pairs and the columns indicate the varying heating scenarios. The range of the colorbar is ± 6000 s. If $\max \mathcal{C}_{AB} < 0.1$, the pixel is masked and colored white.

to longer, positive time lags. These loops are rooted in areas of weaker magnetic field (compared to the center) and thus do not have sufficient energy to evolve significantly into the temperature range of the “hot” component of the 94 Å channel (see Section 2.3). Thus, cooling from 335 Å to the cooler part of 94 Å dominates the cross-correlation. These negative time lags become more prominent as the heating frequency decreases. Consistent with the observations by Viall & Klimchuk (2017) of this same active region, our simulation results for the “cooling” scenario (rightmost column of Figure 8) show negative 94-335 Å time lags of ≈ -2000 s in the longer loops on the lower edge of the active region. However, in other parts of the active region, Viall & Klimchuk found far fewer positive and far more zero 94-335 Å time lags compared to the simulated 94-335 Å time lag maps for any of our heating scenarios.

We also find negative 211-131 Å time lags in the center of the active region for the high-, intermediate-, and low-frequency cases, indicative of plasma cooling from the hot part of the 131 Å channel through the 211 Å channel. Though we have not shown them here, similar negative time lag signatures are present in nearly all of the other 131 Å channel pairs as well. These results are consistent with that of Cadavid et al. (2014) who found that in inter-moss regions of active region NOAA 11250, intensity variations in the 131 Å channel preceded brightenings in all other EUV channels. In

the two control cases, we do not find any negative time lags as the cross-correlations in the core are dominated by uninterrupted cooling from 211 Å to the cool part of 131 Å.

For the 193-171 Å channel pair, we find very few negative time lags because, unlike the 94 and 131 Å channels, the 193 and 171 Å channels are strongly peaked about a single temperature. Along with 211 Å, these channels which are strongly-peaked about a single temperature are important for disambiguating the signals in channels with a bimodal temperature response function (see Figure 11).

In all channel pairs, our simulated time lags show far fewer zero time lags than the observations of Viall & Klimchuk (2012, 2017) and the modeling work of Bradshaw & Viall (2016) due to the lack of transition region emission in our model. Viall & Klimchuk (2015) found that many of the observed zero time lags were not present when observing an active region off the limb, implying that most zero time lags are due to transition region dynamics. Transition region emission shows near-zero time lag because every layer (or temperature) of the transition region responds in unison. However, for the 193-171 Å channel pair, we find that zero time lags still dominate the inner core of the active region for all five heating scenarios, suggesting that the plasma is cooling into, but not through the 171 Å temperature bandpass (Viall & Klimchuk 2017). This underscores the point that zero time lags do not imply steady heating (Viall & Klimchuk 2015, 2016).

3.3.2. Cross-Correlation Maps

Figure 9 shows the peak cross-correlation value, $\max \mathcal{C}_{AB}$, for each selected channel pair. Looking first at all three channel pairs, we see that, on average, the cross-correlation increases as the heating frequency decreases. Additionally, we find that the highest cross-correlations tend to be in the center of the active region while the lowest tend to be on the outer edge. Comparing Figure 9 with the time lags in Figure 8 also reveals that negative time lags are correlated with lower peak cross-correlation values. Furthermore, other than the “cooling” scenario, we find that there are large variations from one loop to the next for all heating frequencies such that the spatial coherence of these peak cross-correlation values is low. In Paper II, we will use the peak cross-correlation value, in addition to the time lag, to classify the heating frequency in each observed pixel.

3.3.3. Histograms

Figure 10 shows histograms of time lags for every channel pair and all five heating scenarios. The time lags are binned between -10^4 s and $+10^4$ s in 60 s bins. Each histogram is colored according the corresponding heating scenario, consistent with Figure 3 and Figure 7. The columns are arranged such that heating frequency decreases from left to right. We show each channel pair for all heating models to demonstrate how the distribution of time lags evolves as the heating frequency varies.

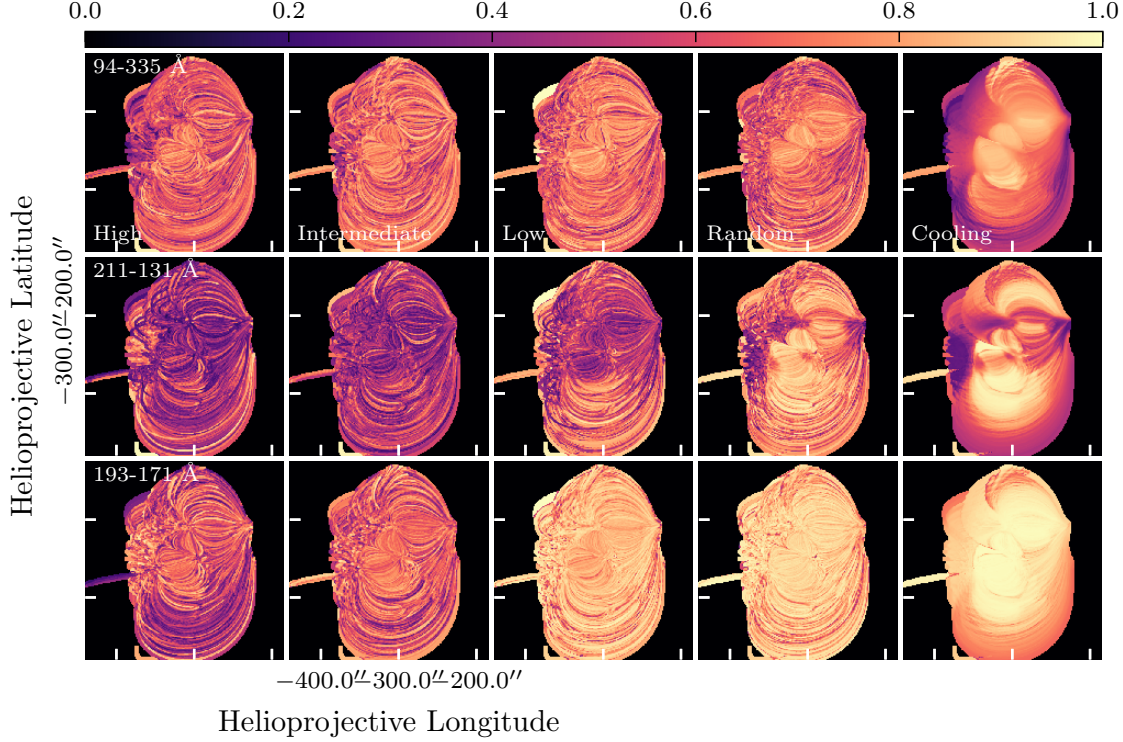


Figure 9. Same as Figure 8 except each pixel shows the maximum cross-correlation, $\max C_{AB}$ (see Equation C5).

Note that as the heating frequency decreases (from left to right), the number of negative time lags decreases. In the “cooling” case, there are very few negative time lags except for channel pairs which include one or both of the double-peaked channels (94 Å and 131 Å). For those channel pairs which include 94 Å and/or 131 Å, we expect to find negative time lags, even in the single-nanoflare cooling case as our convention of ordering the “hot” channel first has been violated such that cooling plasma can lead to negative time lags. For the remaining channel pairs, negative time lags are associated with the heating and cooling cycle being interrupted by repeated events on a given strand.

4. DISCUSSION

For all of our heating models, we find negative time lags in at least one of the three channel pairs as shown in Figure 8. Negative time lags can be used to disambiguate the temperature sensitivity of the AIA passbands and can be produced in one of two ways: high-frequency heating in which the time lag is dominated by many frequent reheatings or a channel pair in which one channel is bimodal. While intensity in the 131 Å channel can correspond to either < 0.4 MK or > 10 MK plasma (see Figure 11), negative time lags in the 211-131 Å channel pair provide a possible signature of ≥ 10 MK plasma because a negative time lag implies the plasma is cooling from 131 Å to 211 Å. This also holds for the 171-131 and 193-131 Å channel pairs as well while the

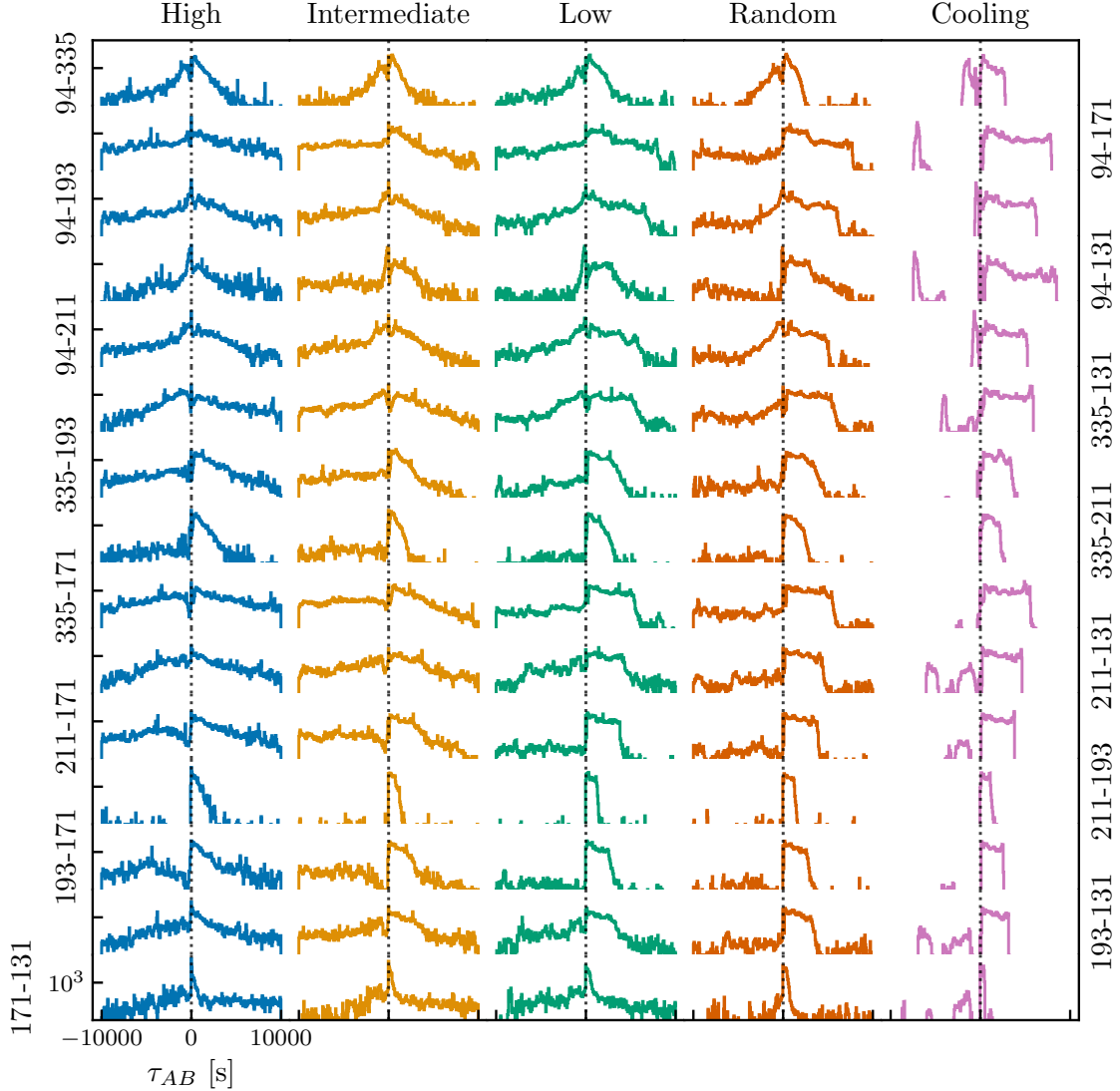


Figure 10. Histograms of time lags across the whole active region. The rows indicate the different channel pairs and the columns indicate the different heating scenarios. Colors are used to denote the various heating scenarios. The black dashed line denotes zero time lag. The bin range is $\pm 10^4$ s and the bin width is 60 s. As with the time lag maps, we do not include time lags corresponding to $\max \mathcal{C}_{AB} < 0.1$.

94-131 and 335-131 Å channels are more ambiguous due to the first channel in the pair being bimodal as well.

As noted in [Section 3.3.1](#), the high-, intermediate-, and low-frequency maps for the 211-131 Å channel pair all show coherent negative time lags in the core. We find far more negative 131 Å time lags here compared to the observed 131 Å time lags of ([Viall & Klimchuk 2017](#)) for this same active region. Because these strands are rooted in areas of strong field, enough energy is made available by the field (see [Section 2.3](#)) to heat them well into (and likely above) the hot component of the 131 Å passband. Since these strands are relatively short, the density increases rapidly enough for this

hot plasma to be visible before it is washed out by thermal conduction. However, given that we are likely not overestimating the total energy budget of the active region (see [Section 3.2](#)), the excess of negative 131 Å time lags seems to imply that the issue may be in the energy distribution. We plan to explore alternative heating scenarios in a future paper.

Plasma undergoing pure cooling by radiation and thermal conduction produces a predictable and well-understood time lag signature. However, complicated heating scenarios and LOS geometries are likely to make it more difficult to interpret observed time lag signatures. Consider the case of a single cooling strand such that the maximum allowed time lag for a given channel pair AB is the amount of time it takes to cool from T_A to T_B by thermal conduction and radiation. We may regard the “cooling” case in [Figure 10](#) as the baseline time lag distribution given that all strands were heated only once at $t = 0$ s. Because the time lag is primarily determined by the cooling phase of the strand, the time lag becomes primarily a function of the loop length L since $\tau_{\text{cool}} \propto L$. Two effects are likely to increase the decoherence of the baseline time lag distribution: multiple structures evolving out-of-phase along a given LOS (the “random” heating scenario) and multiple reheatings before the end of the cooling and draining cycle on a given strand. We note that multiple polluting structures along the LOS seem to primarily add negative time lags to the distribution (the “random” case) while increasing the frequency of events on a given strand extends the distribution in the positive direction. The latter effect also produces more negative time lags. Since steady heating can be thought of as nanoflare heating in the high-frequency limit ($\langle t_{\text{wait}} \rangle \rightarrow 0$), we expect the distribution of time lags to approach a uniform distribution as the heating frequency increases because variations in the intensity will be increasingly dominated by noise ([Viall & Klimchuk 2016](#)). In other words, steadily-heated loops have no preferred time lag.

While our model for the energy deposition (see [Section 2.3](#)) does not assume any specific physical heating mechanism, the parameterization of the heating frequency in [Equation 1](#) has an interesting implication in the context of the [Parker \(1988\)](#) nanoflare model. Rearranging [Equation 1](#) and recalling that $\tau_{\text{cool}} \propto L$ gives $\langle t_{\text{wait}} \rangle \propto L$, i.e. longer strands have longer absolute waiting times between heating events. Given that longer field lines tend to be rooted in regions of weaker magnetic field, this further implies that, where the field is stronger, energy is more quickly dissipated. According to [Parker \(1988\)](#), this dissipation is due to small-scale reconnection of flux tubes that are continually stressed by the convective motion of the underlying photosphere. Thus, in this context, our heating model implies that the reconnection and the underlying driver are more efficient in areas where the field is strongest.

Though we have not addressed it here, another possible mechanism for producing time-varying intensity in active regions is thermal non-equilibrium (TNE) wherein condensation cycles driven by highly-stratified, but steady footpoint heating lead to long-period intensity pulsations ([Kuin & Martens 1982](#)). Though originally used to

explain coronal rain (Antolin et al. 2010, 2015; Auchère et al. 2018) and prominences (Antiochos & Klimchuk 1991), several workers (Mok et al. 2016; Winebarger et al. 2016; Froment et al. 2017; Winebarger et al. 2018; Froment et al. 2018) have recently claimed that TNE can produce time lag signatures similar to those of impulsive heating models, suggesting that observed time lags may be consistent with both impulsive and steady heating. However, it is not yet clear whether TNE is consistent with observed signatures of very hot (8-10 MK) plasma. Detailed comparisons between TNE and nanoflare simulations and observations are desperately needed.

5. SUMMARY

We have carried out a series of numerical simulations in an effort to understand how signatures of the nanoflare heating frequency are manifested in two observables: the emission measure slope and the time lag. Additionally, we described each component of our pipeline for forward modeling active region emission. For a given magnetogram observation of the relevant active region (in this case, NOAA 1158), we compute a potential field extrapolation and trace a large number of field lines through the extrapolated vector field. For each traced field line, we run an EBTEL hydrodynamic simulation and use the resulting temperatures and densities, combined with data from CHIANTI and the instrument response function, to compute the time-dependent intensity. These intensities are then mapped back to the magnetic skeleton and integrated along the LOS in each pixel to create time-dependent images of the active region.

Using our novel and efficient forward modeling pipeline, we produced AIA images for all six EUV channels for ≈ 8 hours of simulation time. From these results, we computed both the emission measure slope and the time lag for all possible channel pairs. We carried out these steps for three different nanoflare heating frequencies, high, intermediate, and low, (see Equation 1) in addition to two control models, for a total of five different heating scenarios (see Table 1).

Our results can be summarized in the following points:

1. As the heating frequency decreases, the emission measure slope, a , becomes increasingly shallow, saturating at $a \approx 2$. As the heating frequency increases, the distribution of slopes over the active region is shifted to higher values and broadens.
2. The time lag becomes increasingly spatially coherent with decreasing heating frequency. When strands are allowed to cool without being re-energized, the spatial distribution of time lags is largely determined by the distribution of loop lengths over the active region.
3. The distribution of time lags becomes increasingly broad as the heating frequency increases, consistent with the results of Viall & Klimchuk (2016).

4. Negative time lags in channel pairs where the second (“cool”) channel is 131 Å provide a possible diagnostic for ≥ 10 MK plasma

In this paper, we have used our advanced forward modeling pipeline to systematically examine how the emission measure slope and time lag are affected by the nanoflare heating frequency. In [Paper II](#), we use the model results presented here to train a random forest classifier and apply it to emission measure slopes and time lags derived from real AIA observations of NOAA 1158. The 15 channel pairs for the time lag and cross-correlation combined with the emission measure slope represent a 31-dimensional feature space and a single 500-by-500 pixel active region amounts to 2.5×10^5 sample points. Performing an accurate assessment over this amount of data manually or “by eye” is at least impractical and likely impossible. Thus, the application of machine learning to the problem of assessing models in the context of real data is a critical step in understanding the underlying energy deposition in active region cores and, to our knowledge, has not yet been applied in this context.

CHIANTI is a collaborative project involving George Mason University (USA), the University of Michigan (USA), University of Cambridge (UK), and NASA Goddard Space Flight Center (USA). This research makes use of SunPy, an open-source and free community-developed solar data analysis package written in Python ([SunPy Community et al. 2015](#)) and PlasmaPy, a community-developed open source core Python package for plasma physics ([PlasmaPy Community et al. 2018](#)). SJB and WTB were supported by the NSF through CAREER award AGS-1450230. The work of NMV was supported by the NASA Supporting Research program. The complete source of this paper, including the data, code, and instructions for running the forward modeling code, can be found at github.com/rice-solar-physics/synthetic-observables-paper-models.

Facility: SDO(AIA,HMI)

Software: Astropy ([The Astropy Collaboration et al. 2018](#)), Dask([Rocklin 2015](#)), IPython([Pérez & Granger 2007](#)), matplotlib([Hunter 2007](#)), Numba([Lam et al. 2015](#)), NumPy([Oliphant 2006](#)), PlasmaPy([PlasmaPy Community et al. 2018](#)), PythonTeX([Poore 2015](#)), seaborn([Waskom et al. 2018](#)), scipy([Jones et al. 2001](#)), Solar-Software([Freeland & Handy 1998](#)), SunPy([Mumford et al. 2018](#)), yt([Turk et al. 2011](#))

APPENDIX

A. NON-EQUILIBRIUM ION POPULATIONS

In order to account for ionization non-equilibrium, we compute $f_{X,k}$ as a function of time t by solving the time-dependent ion population equations for each ion k in each element X ,

$$\frac{\partial f_k}{\partial t} = n_e(R_{k+1}f_{k+1} + I_{k-1}f_{k-1} - I_k f_k - R_k f_k) \quad (\text{A1})$$

where n_e is the electron density and R_k and I_k are the temperature-dependent recombination and ionization rates of ion k , respectively. The ionization and recombination rates are computed using the data provided in CHIANTI. The ionization rates include both direct ionization and excitation autoionization and the recombination rates include both radiative and dielectronic recombination (see section 6 of [Young et al. 2016](#)). Setting the left hand side of [Equation A1](#) to zero gives the equation of ionization equilibrium.

Note that for an element with atomic number Z , we must solve $Z + 1$ coupled differential equations to find the non-equilibrium level populations. Following the approaches of [Masai \(1984\)](#); [Hughes & Helfand \(1985\)](#); [Shen et al. \(2015\)](#), we can write [Equation A1](#) in matrix form,

$$\frac{\partial}{\partial t} \mathbf{F} = \mathbf{A} \mathbf{F}, \quad (\text{A2})$$

where $\mathbf{F} = (f_1, f_2, \dots, f_k, \dots, f_{Z+1})$ and \mathbf{A} is a $Z + 1 \times Z + 1$ tridiagonal matrix containing the ionization and recombination rates, multiplied by the electron density,

$$\mathbf{A} = n_e \begin{pmatrix} -I_1 & R_2 & 0 & \dots & 0 \\ I_1 & -(I_2 + R_2) & R_3 & \dots & 0 \\ & \ddots & \ddots & & \\ \vdots & I_{k-1} & -(I_k + R_k) & R_{k+1} & \vdots \\ & & \ddots & \ddots & \\ 0 & \dots & 0 & I_Z & -R_{Z+1} \end{pmatrix}. \quad (\text{A3})$$

Due to drastic changes in the ionization and recombination rates with temperature, the above system of equations is very “stiff,” making explicit schemes extremely sensitive to the choice of time step ([MacNeice et al. 1984](#); [Bradshaw 2009](#)). To solve [Equation A2](#), we use the “deferred correction” method of [NPL \(1961\)](#), as pointed out by [MacNeice et al. \(1984\)](#),

$$\mathbf{F}_{j+1} = \mathbf{F}_j + \frac{\Delta t}{2} \left(\frac{\partial}{\partial t} \mathbf{F}_{j+1} + \frac{\partial}{\partial t} \mathbf{F}_j \right) + \mathcal{O}(\Delta t^2),$$

where Δt is the time step, j indexes time, and $\mathcal{O}(\Delta t^2)$ denotes terms of second order or higher in Δt . Dropping the higher-order terms and using [Equation A2](#) yields an expression for \mathbf{F}_{j+1} ,

$$\mathbf{F}_{j+1} \approx \left(\mathbb{I} - \frac{\Delta t}{2} \mathbf{A}_{j+1} \right)^{-1} \left(\mathbb{I} + \frac{\Delta t}{2} \mathbf{A}_j \right) \mathbf{F}_j, \quad (\text{A4})$$

where \mathbb{I} is the identity matrix. To solve [Equation A2](#), we need only compute \mathbf{A}_j for each $T(t_j)$, set \mathbf{F}_0 to the equilibrium ion populations, and iteratively compute [Equation A4](#) for all j . We solve [Equation A2](#) for all elements in [Table 2](#) and for each strand in the active region.

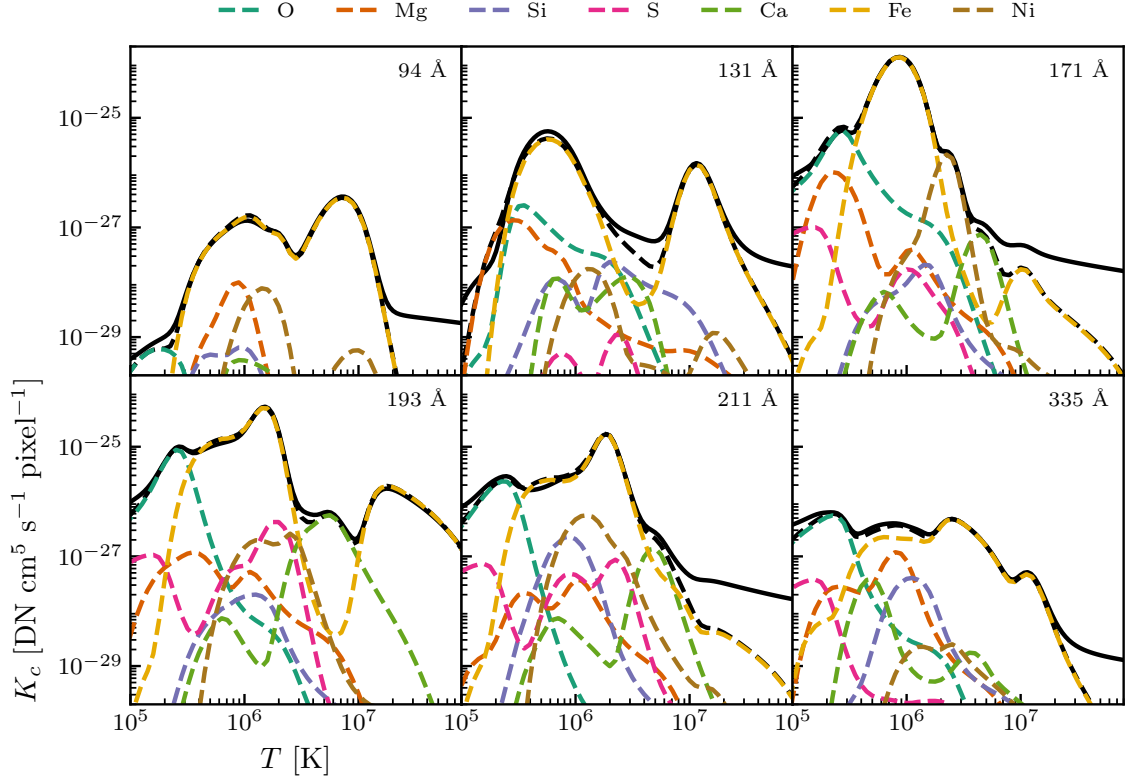


Figure 11. SSW temperature response functions (solid black) and effective temperature response functions for the elements in Table 2 (dashed black) for all six EUV AIA channels. The colored, dashed curves, as indicated in the legend, denote the contributions of the individual elements to the total response. For this calculation, we have assumed equilibrium ionization and a constant pressure of $10^{15} \text{ K cm}^{-3}$. We do not account for the time-varying degradation of the instrument.

Though this method is unconditionally stable, Δt should still be chosen carefully as \mathbf{F} will relax to the equilibrium charge states for very long time steps. In general, smaller time steps should be chosen when the electron temperature varies rapidly and the electron density is high. In this paper, we exploit the adaptive time step provided by the two-fluid EBTEL code which accounts for changes in the temperature and electron density. MacNeice et al. (1984) provide two rules for adaptively adjusting the time step to ensure f_k changes sufficiently slowly. Additionally, Shen et al. (2015) provide an alternate scheme for choosing the time step *a priori* based on the input electron density and the eigenvalues of Equation A3.

B. EFFECTIVE AIA RESPONSE FUNCTIONS

As discussed in Section 2.4.1, the assumption of ionization equilibrium is likely to be violated in the impulsive heating cases considered here. Thus, we must recompute the contributions of each ion to the total channel response, using the result of Equation A2 in place of the equilibrium ion population fractions. Figure 11 shows the effective temperature response functions for the six EUV channels on AIA compared to those

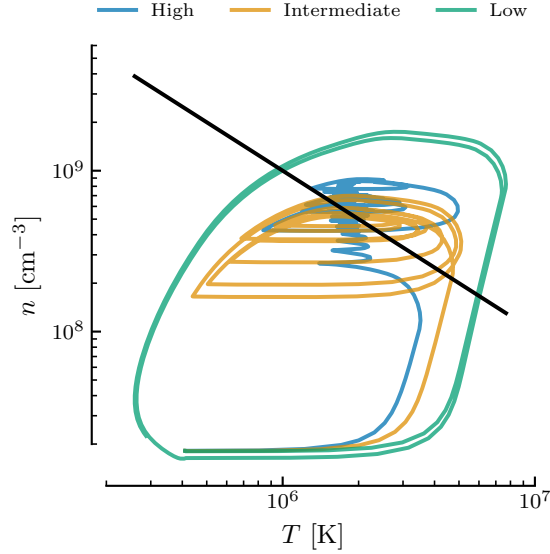


Figure 12. $n - T$ phase-space orbits for a single strand for the three heating scenarios as defined by the legend. The black line indicates a constant pressure of $10^{15} \text{ K cm}^{-3}$.

calculated from `aia_get_response.pro` in SSW. Even though we include a limited number of transitions from the CHIANTI database (see Table 2), we recover nearly all of the response from each channel. The high-temperature contributions in the SSW functions are due to continuum emission which we do not include in our model. In all cases, the continuum contribution is several orders of magnitude below peak of the channel response. Additionally, we do not account for the time variation in the wavelength response functions due to the degradation of the detector (see Section 2.1.6 of Boerner et al. 2012).

Furthermore, during the evolution of a strand, the pressure is not constant for any of our heating scenarios as evidenced by Figure 12. The black line of constant pressure $p = 10^{15} \text{ K cm}^{-3}$ shows the default pressure at which the SSW AIA response functions are evaluated. The other lines show the temperature-density phase space evolution for the high-, intermediate-, and low-frequency cases for a single strand, none of which is well described by the assumption of constant pressure. By recomputing and interpolating the emissivity to the temperatures and densities as defined by our hydrodynamic simulation, we ensure that we are evaluating all quantities in Equation 4 at the correct temperature and density.

C. COMPUTING TIME LAGS

To find the associated time lag for a channel pair in a given pixel, we compute the cross-correlation between the time series associated with each channel and find the delay which maximizes this cross-correlation. We can express the cross-correlation \mathcal{C} between two channels A and B as,

$$\mathcal{C}_{AB}(\tau) = \mathcal{I}_A(t) \star \mathcal{I}_B(t) = \mathcal{I}_A(-t) \star \mathcal{I}_B(t) \quad (\text{C5})$$

where \star and $*$ represent the correlation and convolution operators, respectively, τ is the lag and

$$\mathcal{I}_c(t) = \frac{I_c(t) - \bar{I}_c}{\sigma_c},$$

is the intensity of channel c as a function of time, $I(t)$, centered to zero mean and scaled to unit standard deviation. Taking the Fourier transform, \mathcal{F} , of both sides of Equation C5, using the convolution theorem, and then taking the inverse Fourier transform, \mathcal{F}^{-1} , gives,

$$\begin{aligned} \mathcal{F}\{\mathcal{C}_{AB}(\tau)\} &= \mathcal{F}\{\mathcal{I}_A(-t) * \mathcal{I}_B(t)\}, \\ &= \mathcal{F}\{\mathcal{I}_A(-t)\} \mathcal{F}\{\mathcal{I}_B(t)\}, \\ \mathcal{C}_{AB}(\tau) &= \mathcal{F}^{-1}\{\mathcal{F}\{\mathcal{I}_A(-t)\} \mathcal{F}\{\mathcal{I}_B(t)\}\}. \end{aligned} \quad (\text{C6})$$

Scaling Equation C6 by the length of the intensity time series $I(t)$ yields the same result as that of the correlation defined in Section 2 of Viall & Klimchuk (2012). Furthermore, the *time lag* between channels A and B is defined as,

$$\tau_{AB} = \underset{\tau}{\operatorname{argmax}} \mathcal{C}_{AB}(\tau). \quad (\text{C7})$$

By exploiting the definition of the cross-correlation as given in Equation C6, we can leverage existing Fourier transform algorithms in order to compute \mathcal{C}_{AB} in a scalable and efficient manner. For a 500-by-500 pixel active region observation and 15 possible channel pairs, we need to compute τ_{AB} nearly 4×10^6 times. We use the highly-optimized and thoroughly tested Fourier transform algorithms in the NumPy library for array computations (Oliphant 2006) combined with the Dask library for parallel and distributed computing (Rocklin 2015). Using Dask, we are able to parallelize this operation over many cores such that, on a 64-core machine, we can compute time lags for all 15 channel pairs in every pixel of the active region in less than ten minutes. For comparison, doing the same calculation by calling the IDL function `c_correlate.pro` on each pixel in serial would take ≈ 14 hours for all 15 channel pairs.

REFERENCES

- | | |
|---|--|
| <p>Antiochos, S. K., & Klimchuk, J. A. 1991, ApJ, 378, 372, doi: 10.1086/170437</p> <p>Antolin, P., Shibata, K., & Vissers, G. 2010, ApJ, 716, 154, doi: 10.1088/0004-637X/716/1/154</p> <p>Antolin, P., Vissers, G., Pereira, T. M. D., Rouppe van der Voort, L., & Scullion, E. 2015, ApJ, 806, 81, doi: 10.1088/0004-637X/806/1/81</p> | <p>Auchère, F., Froment, C., Soubrié, E., et al. 2018, ApJ, 853, 176, doi: 10.3847/1538-4357/aaa5a3</p> <p>Barnes, W. T., Bradshaw, S. J., & Viall, N. M. 2019, in prep.</p> <p>Barnes, W. T., Cargill, P. J., & Bradshaw, S. J. 2016a, ApJ, 829, 31, doi: 10.3847/0004-637X/829/1/31</p> <p>—. 2016b, ApJ, 833, 217, doi: 10.3847/1538-4357/833/2/217</p> |
|---|--|

- Boerner, P., Edwards, C., Lemen, J., et al. 2012, *SoPh*, 275, 41, doi: [10.1007/s11207-011-9804-8](https://doi.org/10.1007/s11207-011-9804-8)
- Bradshaw, S. J. 2009, *A&A*, 502, 409, doi: [10.1051/0004-6361/200810735](https://doi.org/10.1051/0004-6361/200810735)
- Bradshaw, S. J., & Cargill, P. J. 2006, *A&A*, 458, 987, doi: [10.1051/0004-6361:20065691](https://doi.org/10.1051/0004-6361:20065691)
- . 2010, *ApJ*, 717, 163, doi: [10.1088/0004-637X/717/1/163](https://doi.org/10.1088/0004-637X/717/1/163)
- Bradshaw, S. J., Klimchuk, J. A., & Reep, J. W. 2012, *ApJ*, 758, 53, doi: [10.1088/0004-637X/758/1/53](https://doi.org/10.1088/0004-637X/758/1/53)
- Bradshaw, S. J., & Viall, N. M. 2016, *ApJ*, 821, 63, doi: [10.3847/0004-637X/821/1/63](https://doi.org/10.3847/0004-637X/821/1/63)
- Brosius, J. W., Daw, A. N., & Rabin, D. M. 2014, *ApJ*, 790, 112, doi: [10.1088/0004-637X/790/2/112](https://doi.org/10.1088/0004-637X/790/2/112)
- Cadavid, A. C., Lawrence, J. K., Christian, D. J., Jess, D. B., & Nigro, G. 2014, *ApJ*, 795, 48, doi: [10.1088/0004-637X/795/1/48](https://doi.org/10.1088/0004-637X/795/1/48)
- Cargill, P. J. 1994, *ApJ*, 422, 381, doi: [10.1086/173733](https://doi.org/10.1086/173733)
- . 2014, *ApJ*, 784, 49, doi: [10.1088/0004-637X/784/1/49](https://doi.org/10.1088/0004-637X/784/1/49)
- Cargill, P. J., Bradshaw, S. J., & Klimchuk, J. A. 2012a, *ApJ*, 752, 161, doi: [10.1088/0004-637X/752/2/161](https://doi.org/10.1088/0004-637X/752/2/161)
- . 2012b, *ApJ*, 758, 5, doi: [10.1088/0004-637X/758/1/5](https://doi.org/10.1088/0004-637X/758/1/5)
- Cargill, P. J., & Klimchuk, J. A. 2004, *ApJ*, 605, 911, doi: [10.1086/382526](https://doi.org/10.1086/382526)
- Cargill, P. J., Mariska, J. T., & Antiochos, S. K. 1995, *The Astrophysical Journal*, 439, 1034, doi: [10.1086/175240](https://doi.org/10.1086/175240)
- Caspi, A., Woods, T. N., & Warren, H. P. 2015, *ApJL*, 802, L2, doi: [10.1088/2041-8205/802/1/L2](https://doi.org/10.1088/2041-8205/802/1/L2)
- Craig, I. J. D., & Brown, J. C. 1976, *A&A*, 49, 239
- Del Zanna, G., & Mason, H. E. 2018, *LRSP*, 15, 5, doi: [10.1007/s41116-018-0015-3](https://doi.org/10.1007/s41116-018-0015-3)
- Del Zanna, G., Tripathi, D., Mason, H., Subramanian, S., & O'Dwyer, B. 2015, *A&A*, 573, A104, doi: [10.1051/0004-6361/201424561](https://doi.org/10.1051/0004-6361/201424561)
- Dere, K. P., Landi, E., Mason, H. E., Fossi, B. C. M., & Young, P. R. 1997, *A&AS*, 125, 25, doi: [10.1051/aas:1997368](https://doi.org/10.1051/aas:1997368)
- Feldman, U., Mandelbaum, P., Seely, J. F., Doschek, G. A., & Gursky, H. 1992, *ApJS*, 81, 387, doi: [10.1086/191698](https://doi.org/10.1086/191698)
- Freedman, D., & Diaconis, P. 1981, *Z. Wahrscheinlichkeitstheorie verw Gebiete*, 57, 453, doi: [10.1007/BF01025868](https://doi.org/10.1007/BF01025868)
- Freeland, S. L., & Handy, B. N. 1998, *SoPh*, 182, 497, doi: [10.1023/A:1005038224881](https://doi.org/10.1023/A:1005038224881)
- Froment, C., Auchère, F., Aulanier, G., et al. 2017, *ApJ*, 835, 272, doi: [10.3847/1538-4357/835/2/272](https://doi.org/10.3847/1538-4357/835/2/272)
- Froment, C., Auchère, F., Mikić, Z., et al. 2018, *ApJ*, 855, 52, doi: [10.3847/1538-4357/aaaf1d](https://doi.org/10.3847/1538-4357/aaaf1d)
- Guarrasi, M., Reale, F., & Peres, G. 2010, *ApJ*, 719, 576, doi: [10.1088/0004-637X/719/1/576](https://doi.org/10.1088/0004-637X/719/1/576)
- Guennou, C., Auchère, F., Klimchuk, J. A., Bocchialini, K., & Parenti, S. 2013, *ApJ*, 774, 31, doi: [10.1088/0004-637X/774/1/31](https://doi.org/10.1088/0004-637X/774/1/31)
- Hannah, I. G., & Kontar, E. P. 2012, *A&A*, 539, A146, doi: [10.1051/0004-6361/201117576](https://doi.org/10.1051/0004-6361/201117576)
- Hughes, J. P., & Helfand, D. J. 1985, *ApJ*, 291, 544, doi: [10.1086/163095](https://doi.org/10.1086/163095)
- Hunter, J. D. 2007, *CSE*, 9, 90, doi: [10.1109/MCSE.2007.55](https://doi.org/10.1109/MCSE.2007.55)
- Ishikawa, S.-n., Glesener, L., Krucker, S., et al. 2017, *NatAs*, 1, doi: [10.1038/s41550-017-0269-z](https://doi.org/10.1038/s41550-017-0269-z)
- Jakimiec, J., Sylwester, B., Sylwester, J., et al. 1992, *Astronomy and Astrophysics*, 253, 269
- Jones, E., Oliphant, T., & Peterson, P. 2001, *SciPy: Open Source Scientific Tools for Python*. <https://www.scipy.org>
- Jordan, C. 1976, *RSPTA*, 281, 391, doi: [10.1098/rsta.1976.0037](https://doi.org/10.1098/rsta.1976.0037)
- Judge, P. G., Hubeny, V., & Brown, J. C. 1997, *ApJ*, 475, 275, doi: [10.1086/303511](https://doi.org/10.1086/303511)

- Judge, P. G., Woods, T. N., Brekke, P., & Rottman, G. J. 1995, *ApJ*, 455, doi: [10.1086/309815](https://doi.org/10.1086/309815)
- Klimchuk, J. A. 2015, *RSPTA*, 373, 20140256, doi: [10.1098/rsta.2014.0256](https://doi.org/10.1098/rsta.2014.0256)
- Klimchuk, J. A., Patsourakos, S., & Cargill, P. J. 2008, *ApJ*, 682, 1351, doi: [10.1086/589426](https://doi.org/10.1086/589426)
- Kuin, N. P. M., & Martens, P. C. H. 1982, *A&A*, 108, L1
- Lam, S. K., Pitrou, A., & Seibert, S. 2015, in *LLVM 2015*, Vol. 7, Proceedings of the Second Workshop on the LLVM Compiler Infrastructure in HPC (New York, NY, USA: ACM), 1–6
- Landi, E., & Klimchuk, J. A. 2010, *ApJ*, 723, 320, doi: [10.1088/0004-637X/723/1/320](https://doi.org/10.1088/0004-637X/723/1/320)
- Lemen, J. R., Title, A. M., Akin, D. J., et al. 2012, *SoPh*, 275, 17, doi: [10.1007/s11207-011-9776-8](https://doi.org/10.1007/s11207-011-9776-8)
- Lionello, R., Alexander, C. E., Winebarger, A. R., Linker, J. A., & Mikić, Z. 2016, *ApJ*, 818, 129, doi: [10.3847/0004-637X/818/2/129](https://doi.org/10.3847/0004-637X/818/2/129)
- MacNeice, P., Burgess, A., McWhirter, R. W. P., & Spicer, D. S. 1984, *SoPh*, 90, 357, doi: [10.1007/BF00173963](https://doi.org/10.1007/BF00173963)
- Masai, K. 1984, *Ap&SS*, 98, 367, doi: [10.1007/BF00651415](https://doi.org/10.1007/BF00651415)
- Mason, H. E., & Fossi, B. C. M. 1994, *A&ARv*, 6, 123, doi: [10.1007/BF01208253](https://doi.org/10.1007/BF01208253)
- Mok, Y., Mikić, Z., Lionello, R., Downs, C., & Linker, J. A. 2016, *ApJ*, 817, 15, doi: [10.3847/0004-637X/817/1/15](https://doi.org/10.3847/0004-637X/817/1/15)
- Mulu-Moore, F. M., Winebarger, A. R., & Warren, H. P. 2011, *ApJL*, 742, L6, doi: [10.1088/2041-8205/742/1/L6](https://doi.org/10.1088/2041-8205/742/1/L6)
- Mumford, S., Christe, S., Mayer, F., et al. 2018, *sunpy/sunpy v0.9.5*, doi: [10.5281/zenodo.2155946](https://doi.org/10.5281/zenodo.2155946). <https://doi.org/10.5281/zenodo.2155946>
- NPL. 1961, *Modern Computing Methods, Notes on Applied Sciences No. 16* (London: National Physical Laboratory, HMSO)
- Oliphant, T. 2006, *A Guide to Numpy* (USA: Trelgol Publishing)
- Parenti, S., del Zanna, G., Petralia, A., et al. 2017, *ApJ*, 846, 25, doi: [10.3847/1538-4357/aa835f](https://doi.org/10.3847/1538-4357/aa835f)
- Parker, E. N. 1988, *ApJ*, 330, 474, doi: [10.1086/166485](https://doi.org/10.1086/166485)
- Pérez, F., & Granger, B. E. 2007, *CSE*, 9, 21, doi: [10.1109/MCSE.2007.53](https://doi.org/10.1109/MCSE.2007.53)
- Pesnell, W. D., Thompson, B. J., & Chamberlin, P. C. 2012, *SoPh*, 275, 3, doi: [10.1007/s11207-011-9841-3](https://doi.org/10.1007/s11207-011-9841-3)
- PlasmaPy Community, Murphy, N. A., Leonard, A. J., et al. 2018, *PlasmaPy*: an open source community-developed Python package for plasma physics, doi: [10.5281/zenodo.1238132](https://doi.org/10.5281/zenodo.1238132). <https://doi.org/10.5281/zenodo.1238132>
- Poore, G. M. 2015, *CS&D*, 8, 014010, doi: [10.1088/1749-4699/8/1/014010](https://doi.org/10.1088/1749-4699/8/1/014010)
- Reale, F., & Orlando, S. 2008, *ApJ*, 684, 715, doi: [10.1086/590338](https://doi.org/10.1086/590338)
- Reep, J. W., Bradshaw, S. J., & Klimchuk, J. A. 2013, *ApJ*, 764, 193, doi: [10.1088/0004-637X/764/2/193](https://doi.org/10.1088/0004-637X/764/2/193)
- Rocklin, M. 2015, in *Proceedings of the 14th Python in Science Conference*, ed. K. Huff & J. Bergstra, 126–132
- Sakurai, T. 1982, *SoPh*, 76, 301, doi: [10.1007/BF00170988](https://doi.org/10.1007/BF00170988)
- Scherrer, P. H., Schou, J., Bush, R. I., et al. 2012, *Solar Physics*, 275, 207, doi: [10.1007/s11207-011-9834-2](https://doi.org/10.1007/s11207-011-9834-2)
- Schmelz, J. T., & Pathak, S. 2012, *ApJ*, 756, 126, doi: [10.1088/0004-637X/756/2/126](https://doi.org/10.1088/0004-637X/756/2/126)
- Schmidt, H. U. 1964, *NASSP*, 50, 107
- Serio, S., Reale, F., Jakimiec, J., Sylwester, B., & Sylwester, J. 1991, *Astronomy and Astrophysics*, 241, 197
- Shen, C., Raymond, J. C., Murphy, N. A., & Lin, J. 2015, *A&C*, 12, 1, doi: [10.1016/j.ascom.2015.04.003](https://doi.org/10.1016/j.ascom.2015.04.003)
- SunPy Community, Mumford, S. J., Christe, S., et al. 2015, *CS&D*, 8, 014009, doi: [10.1088/1749-4699/8/1/014009](https://doi.org/10.1088/1749-4699/8/1/014009)
- The Astropy Collaboration, Price-Whelan, A. M., Sipőcz, B. M., et al. 2018, *AJ*, 156, 123, doi: [10.3847/1538-3881/aabc4f](https://doi.org/10.3847/1538-3881/aabc4f)

- Thompson, W. T. 2006, *A&A*, 449, 791,
doi: [10.1051/0004-6361:20054262](https://doi.org/10.1051/0004-6361:20054262)
- Tripathi, D., Klimchuk, J. A., & Mason, H. E. 2011, *ApJ*, 740, 111,
doi: [10.1088/0004-637X/740/2/111](https://doi.org/10.1088/0004-637X/740/2/111)
- Turk, M. J., Smith, B. D., Oishi, J. S., et al. 2011, *ApJS*, 192, 9,
doi: [10.1088/0067-0049/192/1/9](https://doi.org/10.1088/0067-0049/192/1/9)
- Viall, N. M., & Klimchuk, J. A. 2011, *ApJ*, 738, 24,
doi: [10.1088/0004-637X/738/1/24](https://doi.org/10.1088/0004-637X/738/1/24)
- . 2012, *ApJ*, 753, 35,
doi: [10.1088/0004-637X/753/1/35](https://doi.org/10.1088/0004-637X/753/1/35)
- . 2015, *ApJ*, 799, 58,
doi: [10.1088/0004-637X/799/1/58](https://doi.org/10.1088/0004-637X/799/1/58)
- . 2016, *ApJ*, 828,
doi: [10.3847/0004-637X/828/2/76](https://doi.org/10.3847/0004-637X/828/2/76)
- . 2017, *ApJ*, 842, 108,
doi: [10.3847/1538-4357/aa7137](https://doi.org/10.3847/1538-4357/aa7137)
- Warren, H. P., Brooks, D. H., & Winebarger, A. R. 2011, *ApJ*, 734, 90,
doi: [10.1088/0004-637X/734/2/90](https://doi.org/10.1088/0004-637X/734/2/90)
- Warren, H. P., Winebarger, A. R., & Brooks, D. H. 2012, *ApJ*, 759, 141,
doi: [10.1088/0004-637X/759/2/141](https://doi.org/10.1088/0004-637X/759/2/141)
- Waskom, M., Botvinnik, O., O’Kane, D., et al. 2018, *mwaskom/seaborn* v0.9.0,
doi: [10.5281/zenodo.1313201](https://doi.org/10.5281/zenodo.1313201). <https://doi.org/10.5281/zenodo.1313201>
- Winebarger, A. R., Lionello, R., Downs, C., Mikić, Z., & Linker, J. 2018, *ApJ*, 865, 111,
doi: [10.3847/1538-4357/aad9fb](https://doi.org/10.3847/1538-4357/aad9fb)
- Winebarger, A. R., Lionello, R., Downs, C., et al. 2016, *ApJ*, 831, 172,
doi: [10.3847/0004-637X/831/2/172](https://doi.org/10.3847/0004-637X/831/2/172)
- Winebarger, A. R., Schmelz, J. T., Warren, H. P., Saar, S. H., & Kashyap, V. L. 2011, *ApJ*, 740, 2,
doi: [10.1088/0004-637X/740/1/2](https://doi.org/10.1088/0004-637X/740/1/2)
- Winebarger, A. R., Warren, H. P., Schmelz, J. T., et al. 2012, *ApJL*, 746, L17, doi: [10.1088/2041-8205/746/2/L17](https://doi.org/10.1088/2041-8205/746/2/L17)
- Withbroe, G. L., & Noyes, R. W. 1977, *ARA&A*, 15, 363, doi: [10.1146/annurev.aa.15.090177.002051](https://doi.org/10.1146/annurev.aa.15.090177.002051)
- Young, P. R., Dere, K. P., Landi, E., Zanna, G. D., & Mason, H. E. 2016, *JPhB*, 49, 074009,
doi: [10.1088/0953-4075/49/7/074009](https://doi.org/10.1088/0953-4075/49/7/074009)